# Observation of Gauge Field-Induced Non-Hermitian Helical Skin Effects

Yu-Hong Han(韩宇宏)[1†], Yi Li(李一)[1†], Jia-Hui Zhang(张佳辉)[1], Yang Kou(寇杨)[1], Liantuan Xiao(肖连团)[1,2], Suotang Jia(贾锁堂)[1,2], Linhu Li(李林虎)[3*], and Feng Mei(梅锋)[1,2*]

[1]*State Key Laboratory of Quantum Optics Technologies and Devices, Institute of Laser Spectroscopy, Shanxi University, Taiyuan 030006, China*

[2]*Collaborative Innovation Center of Extreme Optics, Shanxi University of Taiyuan, Taiyuan 030006, China*

[3]*Quantum Science Center of Guangdong-Hong Kong-Macao Greater Bay Area (Guangdong), Shenzhen 518045, China*

(Received 13 December 2025; accepted manuscript online 27 February 2026)

Synthetic gauge fields and non-Hermitian skin effects are central to topological phases and non-Hermitian physics, and each has recently attracted considerable interest across diverse research areas. Realizing skin effects typically requires asymmetric coupling or on-site gain and loss. Here, we theoretically and experimentally show that, under gauge fields, symmetry dissipative couplings can generate a nonreciprocal skin effect with a pseudospin degree of freedom and helical transport, which we term the "helical pseudospin skin effect". Before introducing gauge fields, the model exhibits localized pseudospin edge modes and extended bulk modes without skin effects. As the gauge field strength increases from 0 to $\pi$, we observe the emergence of a non-Hermitian topological phase transition between hybrid- and second-order helical pseudospin skin effects. Our findings highlight gauge-field-enriched non-Hermitian topology and introduces pseudospin-dependent accumulation into skin effects.

DOI: 10.1088/0256-307X/43/4/040704 CSTR: 32039.14.0256-307X.43.4.040704

*1. Introduction.* Non-Hermitian physics has recently attracted significant attention by revealing behaviors not possible in conservative Hermitian systems.[1,2] In particular, the non-Hermitian skin effect (SE) is especially intriguing because it causes wave modes to localize at boundaries rather than remain distributed throughout the bulk.[3–14] This effect has profound implications for the development of innovative wave-based technologies, including wave morphing,[15–17] topological lasers,[18] and advanced sensors.[19,20] Consequently, experimental realizations have been actively pursued across a wide range of wave systems, including photonic,[21–28] acoustic,[29–42] circuit,[43–50] transmission line,[51] and quantum systems.[52–57] Notably, implementing non-Hermitian SEs usually requires unequal left–right coupling strengths or on-site gain and loss,[58–60] which directly or effectively introduce asymmetry in wave propagation and lead to the accumulation of wave modes at one boundary. Very recently, two studies showed that nonreciprocity and SEs can also arise in reciprocal bilayer systems with symmetric dissipative couplings.[41,42]

Meanwhile, recent years have seen growing interest in realizing both Abelian[61–67] and non-Abelian synthetic gauge fields.[68–70] These artificial fields mimic the effects of real gauge fields on charge-neutral classical waves and can give rise to novel topological phenomena such as Brillouin–Klein bottles,[71] chiral zero modes,[72–75] and Stiefel–Whitney topological phases.[76] From an applications perspective, such fields also provide new mechanisms for controlling wave propagation, enabling phenomena such as gauge field-induced Landau rainbows,[77] Anderson localization,[78–80] negative refraction,[81,82] broadband wave routing,[83] and robust transport.[84–86]

In this work, we theoretically and experimentally demonstrate that combining synthetic gauge fields and reciprocal dissipative couplings not only induces nonreciprocity and SEs but also enables control over their accumulation directions and associated non-Hermitian topological phase transitions. As illustrated in Fig. 1, before the application of the gauge fields, the model hosts localized pseudospin edge modes and extended bulk modes without SEs. When a gauge field is introduced and its phase increases from 0 to $\pi$, the pseudospin-up and -down skin modes accumulate toward opposite edges, displaying spin-dependent accumulation directions. Reversing the sign of the gauge field phase flips these accumulation directions, giving rise to what we term the helical pseudospin skin effect (HSE). Moreover, varying the gauge field phase drives a non-Hermitian topological phase transition between hybrid- and second-order HSEs. Experimentally, we implement synthetic gauge fields and reciprocal dissipative couplings in circuit metamaterials, measure the non-Hermitian spectral topological invariants, and observe the predicted helical accumulation of pseudospin skin modes. Compared with previous works, our study establishes an alternative platform based on synthetic gauge fields and dissipative couplings for inducing and controlling SEs without requiring explicitly engineered nonreciprocal couplings.

†These authors contributed equally to this work.
*Corresponding authors. Email: lilinhu@quantumsc.cn; meifeng@sxu.edu.cn

© 2026 Chinese Physical Society and IOP Publishing Ltd. All rights, including for text and data mining, AI training, and similar technologies, are reserved.

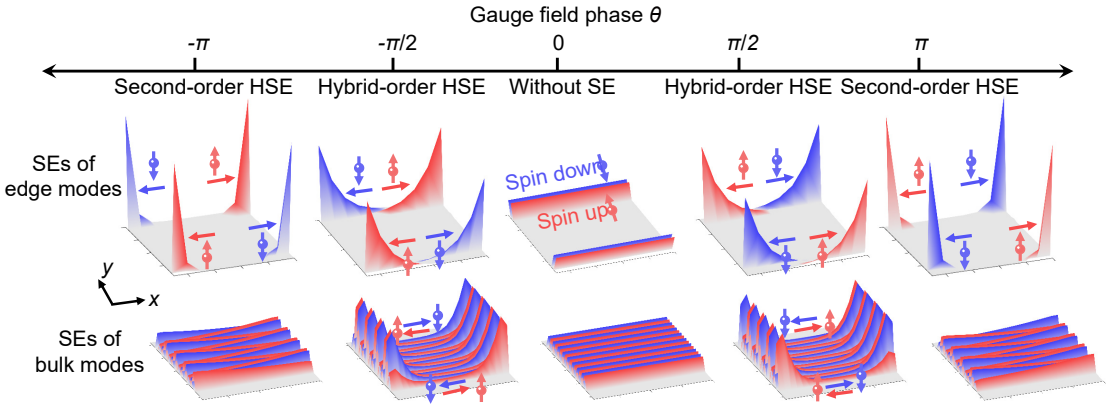


**Fig. 1.** Schematic of HSEs induced and enriched by gauge fields. In a non-Hermitian system with reciprocal couplings and without on-site gain and loss, nonreciprocal SEs are generally not expected. This work shows that introducing gauge fields into such a system can induce nonreciprocal HSEs. For zero gauge field ($\theta = 0$), the system hosts localized pseudospin edge modes and extended bulk modes, while no SEs are observed. When the gauge field is turned on ($\theta > 0$), the pseudospin-up and -down eigenmodes accumulate toward opposite corners or edges of the $x$-direction, regardless of whether they are edge or bulk modes, resulting in hybrid-order HSEs. When $\theta = \pi$, the pseudospin-up and -down edge modes continue collapsing toward opposite corners, while the bulk modes begin to delocalize, leading to second-order HSEs. Reversing the sign of the gauge field phase can flip the directions of the HSEs.

*2. Gauge Field Induced HSEs.* Concretely, we consider a two-dimensional bilayer lattice model, as depicted in Fig. 2(a), where each unit cell contains four sites. The momentum-space Hamiltonian can be written as

$$\begin{aligned} H =& -2it_3\cos k_x\sigma_0\tau_0 + (t_1 + t_2\cos k_y)\sigma_0\tau_x \\ &+ t_2\sin k_y\sigma_0\tau_y + t_3\left(\sin k_x - \sin(k_x+\theta)\right)\sigma_y\tau_z \\ &+ t_3\left(\cos k_x + \cos(k_x+\theta)\right)\sigma_x\tau_z, \end{aligned} \tag{1}$$

where $\tau_{x,y,z}$ and $\sigma_{x,y,z}$ denote the Pauli matrices acting on the sublattice space (a, b) or (c, d) and the upper- and lower-layer degrees of freedom, respectively. $t_1$ represents the intra-unit-cell couplings, $t_2$ the inter-unit-cell couplings, and $-it_3$ the reciprocal dissipative couplings that introduce non-Hermiticity while maintaining equal left–right coupling strengths. Parameter $\theta$ denotes the gauge field phase applied to the interlayer couplings. Despite the presence of gauge fields, the non-Hermitian bilayer system preserves a gauge-field-dependent mirror symmetry, expressed as $\mathcal{M}_z H(k_x,k_y)\mathcal{M}_z^{-1} = H(k_x,k_y)$, where the mirror symmetry operator is $\mathcal{M}_z = G\sigma_x\tau_0$, with $\mathcal{M}_z^2 = 1$, $G = \cos(\theta/2)\sigma_0\tau_0 + \mathrm{i}\sin(\theta/2)\sigma_z\tau_0$ representing the gauge-field-dependent symmetry transformation.

Since $[\mathcal{M}_z, H] = 0$, the Bloch Hamiltonian, $H$ can be block diagonalized in the eigenspace of $\mathcal{M}_z$. We refer to the eigenvector spaces of $\mathcal{M}_z$ as pseudospin spaces, with eigenvalues $\pm1$ corresponding to the pseudospin-up and -down subspaces, respectively. Within these subspaces, the Bloch Hamiltonian block-diagonalizes into $H_+ \oplus H_-$, where $+$ and $-$ denote the pseudospin-up and -down sectors, respectively. Accordingly, the pseudospin-up and -down labels in Figs. 2–4 correspond to results obtained within these pseudospin subspaces. The block Hamiltonian takes the following form:

$$\begin{aligned} H_\pm(k) =& -2it_3\cos k_x\tau_0 + (t_1 + t_2\cos k_y)\tau_x \\ &+ t_2\sin k_y\tau_y \pm 2t_3\cos\left(k_x + \frac{\theta}{2}\right)\tau_z. \end{aligned} \tag{2}$$

The effective nonreciprocity in the pseudospin basis arises from interference between dissipative intra- and inter-layer couplings. Notably, $H_\pm$ exhibit a periodicity of $4\pi$ in the gauge field phase (i.e., $H_\pm(k_x,k_y,\theta) = H_\pm(k_x,k_y,\theta+4\pi)$. The pseudospin-up and -down subspace Hamiltonians are related by $H_\pm(k_x,k_y,\theta) = H_\mp(k_x,k_y,\theta+2\pi)$. This property ensures that the pseudospin-up and -down SEs display pseudospin-rotational symmetry under a gauge-field phase shift of $2\pi$. In Section IV of the Supplementary Material, we further show that the absence and emergence of SEs at gauge field phases $\theta = 0, \pm\pi$ can be attributed to the time-reversal symmetry properties of the Bloch Hamiltonian.[87] Notably, our use of mirror symmetry mainly serves as an intuitive framework for understanding the HSEs. The effect itself is a general and robust phenomenon that does not rely strictly on mirror symmetry. To support this point, as shown in Section II of the Supplementary Material, we consider two representative perturbations: mirror-symmetry-preserving perturbations applied to the dissipative coupling terms and a staggered mass term that explicitly breaks mirror symmetry. We find that the HSE remains robust against both types of perturbations. Moreover, the HSE is not limited to mirror symmetry and can emerge under other symmetry constraints, such as rotational symmetry.

The emergence of SEs can be characterized by the geometric features of energy spectra for bulk and edge modes.[88,89] In Fig. 2(b), we examine the energy spectra under three types of boundary conditions with varying gauge field phases. Under Case (i), the spectra consist only of two gapped bulk bands corresponding to eigenenergies with positive and negative Re[$E$]. In contrast, for Cases (ii) and (iii) under OBC, additional in-gap edge bands appear between the two bulk bands. As discussed below, the spectral distinction between Cases (ii) and (iii) allows us to distinguish SEs associated with edge modes from those associated with bulk modes.

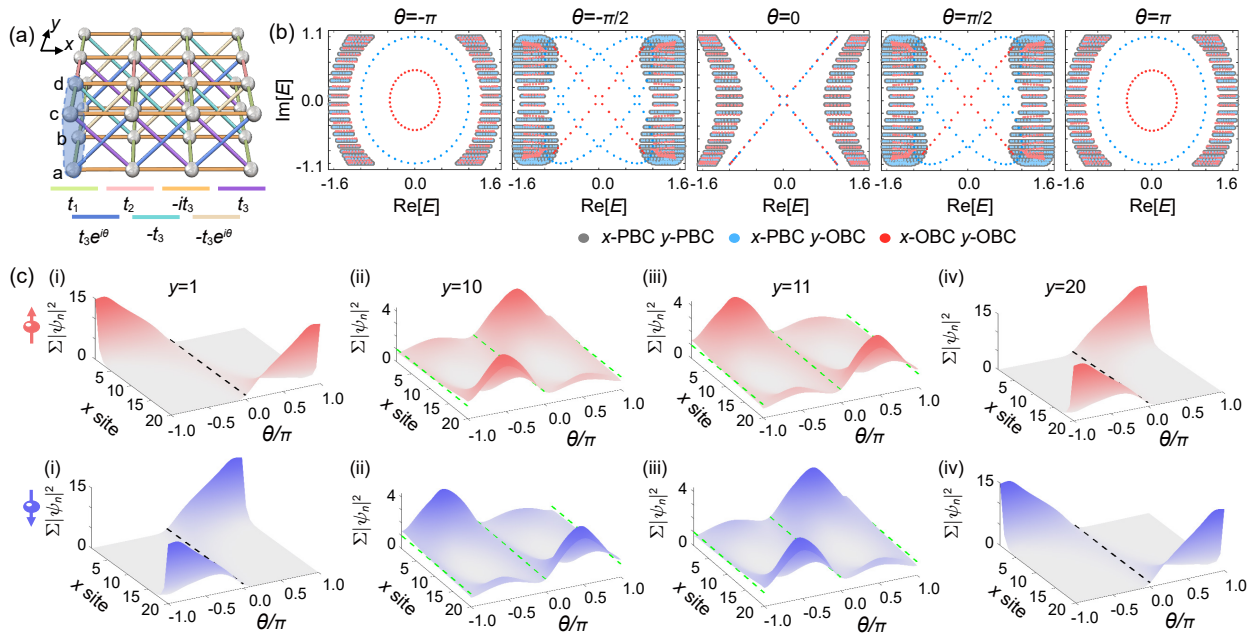


**Fig. 2.** Model and helical SEs. (a) Non-Hermitian lattice model with reciprocal dissipative couplings $-it_3$ and synthetic gauge fields $e^{i\theta}$. (b) Energy spectra under different boundary conditions for five distinct gauge field phases. (c) Density distributions of all pseudospin-up and -down modes as a function of $\theta$ for four different $y$. The black and green dashed lines indicate the points where the SE vanishes for edge and bulk modes, respectively. As shown, with increasing $\theta$, the pseudospin-up and -down skin modes exhibit helical evolution along the $x$-direction. The parameters are $t_1 = 0.22t_2$, $t_3 = 0.5t_2$, $N_x = 20$, and $N_y = 10$.

Specifically, at $\theta = \pm\pi$, in Cases (ii) and (iii), the geometries of the bulk bands remain identical, whereas the edge bands shrink from a larger circle to a smaller one. This behavior indicates that the edge modes exhibited SE, while the bulk modes do not. As depicted in Fig. 2(c), all edge modes are maximally localized at the corners of the two-dimensional lattice, giving rise to a second-order SE.[90] When the gauge field phase is tuned to $\theta = \pm\pi/2$, the geometries of the bulk and edge bands become distinct under different boundary conditions, indicating the coexistence of SEs in both. In this regime, the SE of edge modes persists at the corners, corresponding to second-order SE, while the SE of bulk modes appears along the edges [see Fig. 2(c)], corresponding to conventional first-order SE. Together, they form a hybrid-order SE. In contrast, at $\theta = 0$, the spectra are identical for Cases (ii) and (iii), indicating the absence of any SE.

To reveal the spin-dependent helical features of the SEs, figure 2(c) shows the density distribution, $\sum|\psi_n|^2$ of both edge and bulk eigenmodes as a function of the gauge field phase, $\theta$, evaluated at the lower edge ($y = 1$), bulk sites ($y = 10, 11$), and the upper edge ($y = 20$). Here, $\psi_n$ denotes eigenmodes in different pseudospin subspaces. For pseudospin-up modes on the lower edge, a left SE appears at $\theta = -\pi$, gradually weakens as $\theta$ increases, and vanishes at the critical point, $\theta = 0$. Beyond this point, the right SE emerges and reaches a maximum at $\theta = \pi$. The upper edge exhibited the opposite evolution: the SE begins on the right, disappears at $\theta = 0$, and reappears on the left at $\theta = \pi$. The bulk modes display a richer pattern. Their SE direction depends on the $y$-coordinate: for even $y$ (e.g., $y = 10$), the SE switches from right- to left-moving as $\theta$ crosses 0, whereas odd $y$ values display the opposite trend. For pseudospin-down modes, the SE intensity follows the same phase dependence, but the propagation direction is reversed relative to pseudospin-up. These observations confirm that the SEs exhibit gauge-field-induced helical evolution. In Section I of the Supplementary Material, we present the real-space distributions of both bulk and boundary modes as the gauge field phase, $\theta$ varies, providing a direct visualization of the gauge-field-induced helical SE.

The topology of the HSEs in the edge and bulk modes can be characterized by the following topological winding number:[3]

$$W = \frac{1}{2\pi \mathrm{i}} \oint_{-\pi}^{\pi} \frac{\partial}{\partial k_x} \log\left[E(k_x) - E_r\right] \mathrm{d}k_x, \tag{3}$$

where $E(k_x)$ denotes the energy spectrum under $x$-PBC and $y$-OBC, and $E_r$ is a reference energy. For any reference energy, $E_r$ located inside the closed loop of eigenenergies, the winding number takes a nontrivial value, $W \neq 0$. This winding number characterizes the direction of the exponential decay of the eigenmode wavefunctions associated with the spectral loop and therefore determines the direction of the SE. Moreover, the presence or absence of spectral winding in the bulk and boundary spectra provides a direct criterion for identifying the order of the SE. Specifically, a nonzero winding that appearing simultaneously in both bulk and boundary spectra corresponds to a hybrid-order SE. In contrast, when the bulk winding vanishes while a nonzero winding remains only in the boundary spectrum, the SE is classified as a second-order winding. In Section I of the Supplementary Material, we provide a phase diagram mapping the winding numbers

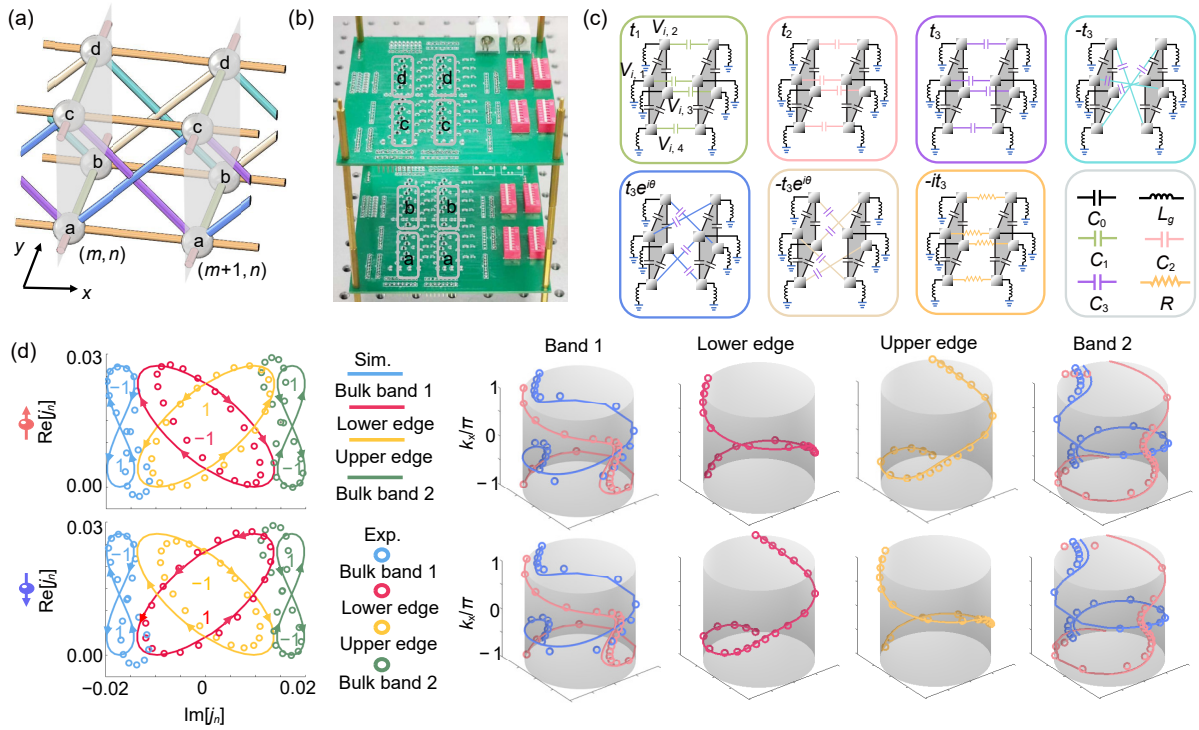


**Fig. 3.** Implementation of synthetic gauge fields and measurement of topological winding numbers. (a) Schematic of the couplings between two unit cells. The coordinates for each unit cell are labelled as $(m, n)$. (b) The corresponding printed circuit board. (c) Specific circuit connections for implementing $t_1$, $t_2$, $\pm t_3$, $\pm t_3 e^{i\theta}$ and $-it_3$ to implement the gauge field phase $\theta = \pi/2$. (d) The left panel shows measured (circles) and simulated (lines) energy spectra under $x$-PBC and $y$-OBC at $\theta = \pi/2$, while the right panel presents the corresponding three-dimensional illustration of the spectral winding topology.

and corresponding skin-effect orders as a function of the gauge field phase, $\theta$.

As a representative point in this phase diagram, for $\theta = 0.5\pi$, the energy spectrum under $x$-PBC and $y$-OBC forms closed loops in both the pseudospin-up and -down subspaces, as shown in Fig. 3(d). As illustrated on the right side of Fig. 3(d), the sign of the winding numbers is determined by the winding direction as a function of $k_x$. For each pseudospin, the two bulk bands (blue and green) simultaneously exhibit winding numbers $W = \pm 1$, producing left and right SEs of bulk modes. In contrast, for pseudospin-up edge bands, the lower edge band (red) exhibits $W = -1$ (right SE of edge modes), while the upper band (yellow) exhibits $W = 1$ (left SE of edge modes). For pseudospin-down edge bands, the situation is reversed: the lower band exhibits a left SE ($W = 1$), and the upper band exhibits a right SE ($W = -1$). Because nonzero spectral winding appears simultaneously in both the bulk and boundary spectra, this case corresponds to a hybrid-order SE. Notably, although the eigenenergies are affected by measurement errors, the winding behavior remains clearly observable.

*3. Experimental Implementation.* Next, we implement the lattice model under various gauge field phases using circuit metamaterials.[91–95] Here, we focus on realizing the $\theta = \pi/2$ configuration using the basic two-unit-cell building block shown in Fig. 3(a), while the circuit designs for other phases ($\theta = 0, \pm\pi/3, -\pi/2, \pm 2\pi/3, \pm\pi$) are provided in Section VI of the Supplementary Material. The fabricated PCB and mapping between the circuit network and lattice couplings are presented in Figs. 3(b) and 3(c). To encode the complex hopping amplitudes required by the gauge field, each lattice site is represented by four circuit nodes coupled through capacitors and grounded through inductance $L_g$. The intra- and inter-cell couplings, $t_1$, $t_2$, and $t_3$ are implemented by capacitors $C_1$, $C_2$, and $C_3$, respectively, while the phase-dependent hoppings ($-t_3$, $\pm t_3 e^{i\pi/2}$) are generated through cross connections between the corresponding nodes. Reciprocal dissipative couplings proportional to $-it_3$ are realized using resistive links. To validate the circuit design, we derive the eigen-equation using Kirchhoff's law. By driving the quadrangle with the composite excitation $\boldsymbol{V}_i = V_{i,1} + e^{-i\pi/2} V_{i,2} + e^{i\pi} V_{i,3} + e^{i\pi/2} V_{i,4}$, the response satisfies $\boldsymbol{I}_\alpha(\omega) = \sum_\beta J_{\alpha\beta}(\omega) \boldsymbol{V}_\beta(\omega)$, where $J(\omega)$ is the circuit Laplacian. At the resonant frequency, $\omega_0 = 1/\sqrt{(C_1 + C_2 + 2C_3 + 2C_0) L_g}$, The Laplacian $J(\omega_0)$ reproduces the non-Hermitian Hamiltonian of Fig. 2(a) for $\theta = \pi/2$ (see Section VI of the Supplementary Material).

*4. Observation of HSEs.* To further investigate the pseudospin SE and its helical transport behavior as the gauge field varies, the circuit metamaterial is configured with $x$-OBC and $y$-OBC, consisting of $8 \times 8$ nodes. By diagonalizing the measured impedance matrix, $G$ to obtain the eigenvectors, $|\psi_n\rangle$, we track the density distributions of edge and bulk wavefunctions as functions of the gauge field phase, $\theta$. Specifically, the measured and simulated results for the edge modes in the gauge field phases,

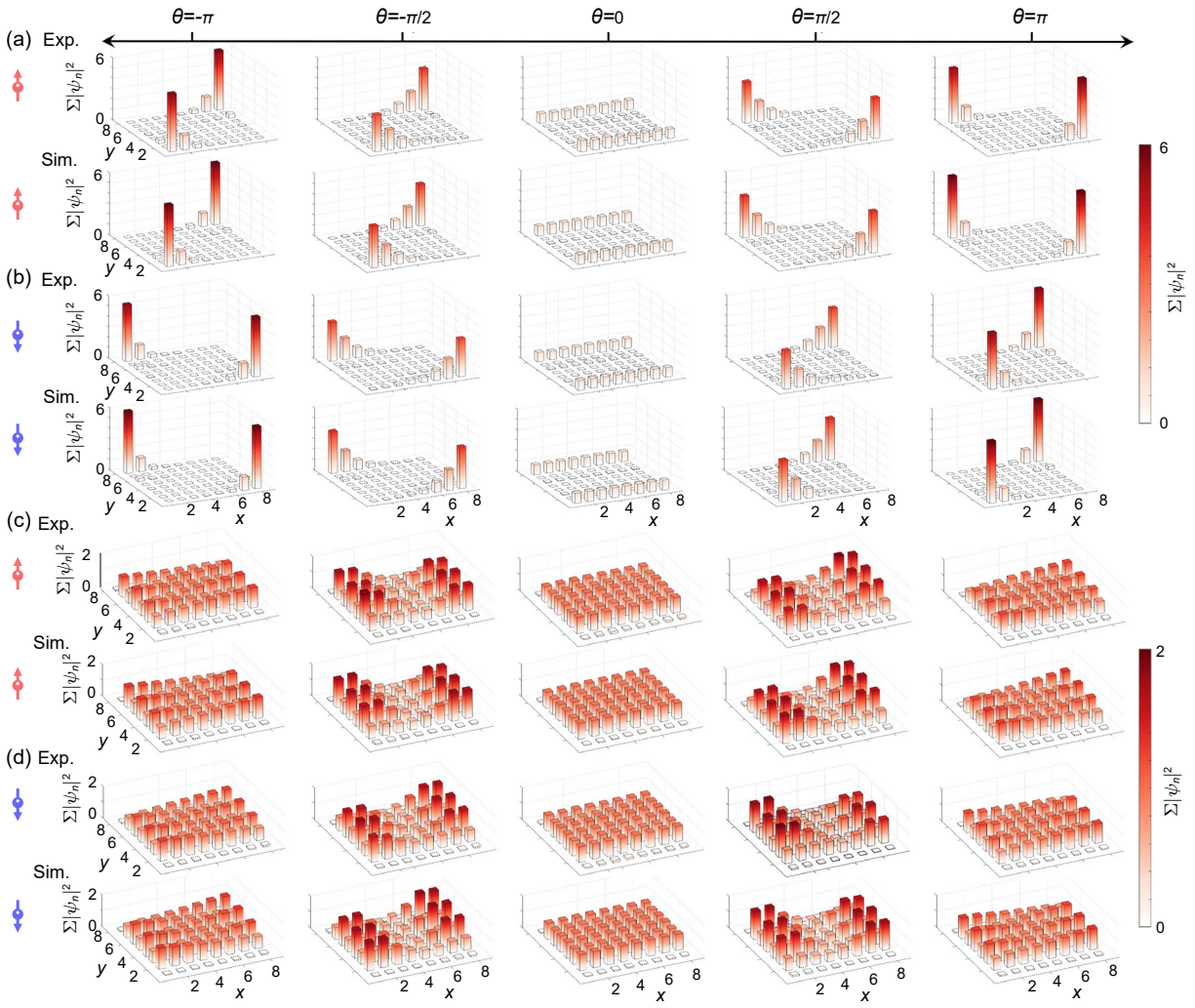


**Fig. 4.** Observation of non-Hermitian HSEs. Measured and simulated density distributions for pseudospin-up (a) and pseudospin-down (b) edge modes as the gauge field phases varies $\theta = -\pi, -\pi/2, 0, \pi/2, \pi$. (c, d) Same as (a, b) but for bulk modes. As shown, for $\theta = 0$, the system exhibits no SE. For $\theta = \pm\pi/2$, the system exhibits a hybrid-order HSE in which pseudospin-up and -down edge and bulk modes localize at opposite boundaries. At $\theta = \pm\pi$, the system transitions to a second-order HSE, where only edge modes remain localized.

$\theta = 0, \pm\pi/2, \pm\pi$ are shown in Figs. 4(a) and 4(b), while those for the bulk modes are shown in Figs. 4(c) and 4(d). The results for other gauge field phases, $\theta = \pm\pi/3, \pm 2\pi/3$ are provided in Section VII of the Supplementary Material.

As shown, for the pseudospin-up edge modes at $\theta = -\pi$, the lower edge exhibits a left SE, while the upper edge displays a right SE. As the gauge field phase, $\theta$ increases to $-\pi/2$, although the SE directions at both the lower and upper edges remain unchanged, their strengths are reduced. When $\theta = 0$, the left and right SEs vanish completely, and the edge modes become localized across the system, indicating a phase in which the system exhibits no SE of edge modes. As the flux increases further to $\theta = \pi/2$, the direction of the SEs reverse compared with those at $\theta = -\pi/2$: the lower edge now exhibits a right SE, and the upper edge exhibits a left SE, indicating that the edge-mode localization has flipped to the opposite side of the system. At $\theta = \pi$, this reverse localization becomes stronger than at $\theta = \pi/2$. For the pseudospin-down edge modes, the overall behavior is similar to that of the pseudospin-up modes, but with the opposite SE direction at each stage. For example, when $\theta = -\pi$, the upper edge exhibits a left SE, and the lower edge exhibits a right SE. This reversal of SE direction for pseudospin-down modes relative to pseudospin-up modes, demonstrates a clear helical pseudospin-dependent feature. Small discrepancies between measured and simulated density distributions are attributed to measurement errors. Notably, the eigenmode measurements exhibit smaller deviations than the winding-number measurements in Fig. 3(d), reflecting the greater robustness of the eigenmodes against perturbations.

For the pseudospin-up bulk modes at $\theta = -\pi$, no SE is observed; the bulk modes are evenly distributed across the system, indicating the absence of SE for bulk modes. As the gauge field increases to $\theta = -\pi/2$, an intriguing behavior emerges: the bulk modes exhibit a left SE for odd $y$ coordinates and a right SE for even $y$ coordinates, forming a pattern of alternating localization across the lattice. At $\theta = 0$, the SE vanishes again, and the bulk modes

return to an even distribution. As the flux increases further to $\theta = \pi/2$, the localization pattern reappears, but with reversed directions: odd $y$ coordinates exhibit a right SE, while even $y$ coordinates show a left SE. Finally, at $\theta = \pi$, the SE disappears once more, and the bulk modes again become evenly distributed, like the observation at $\theta = 0$ and $\theta = -\pi$. For the pseudospin-down bulk modes, the behavior is similar to that of the pseudospin-up bulk modes, but in the opposite SE direction.

The combined experimental observations of SEs for both bulk and edge modes clearly demonstrate that when the gauge field phase, $\theta \in (0, \pi)$, a hybrid-order HSE emerges, characterized by HSEs of both edge and bulk modes. When $\theta = \pi$, only HSEs of edge modes remain, while those of bulk HSEs disappear, giving rise to second-order HSEs. Furthermore, the direction of the SEs induced by the gauge field depends helically on the pseudospin degree of freedom, analogous to the helical pseudospin edge states found in the time-reversal-invariant TI phases, leading to the emergence of HSEs. Moreover, the helical direction can be reversed by changing the sign of the gauge field phase. In Section VIII of the Supplementary Material, we further demonstrate that such HSE can be exploited to realize pseudospin-dependent nonreciprocality and to design one-wave spintronic transport.

*5. Discussion.* In summary, we have theoretically and experimentally demonstrated a mechanism for inducing SEs based on the combination of synthetic gauge fields and symmetry dissipative couplings. We show that tuning the gauge field phase not only produces helical, pseudospin-dependent accumulation of SEs, but also drives a non-Hermitian topological phase transition between two distinct two-dimensional pseudospin SEs. These findings may be of broad interest to the photonics, condensed matter, and metamaterials communities. Looking ahead, given the recent realization of synthetic Abelian and non-Abelian gauge fields across a wide range of classical and quantum platforms,[61,66,68,69] our study provides timely insights into gauge-field-enriched non-Hermitian topological phases and SEs and opens pathways for potential technological applications, such as gauge-field-engineered and spin-dependent one-way quantum transport.

*Acknowledgements.* We acknowledge Profs. Jing Zhang, Z.D. Wang, Yu-Xin Zhao, Luqi Yuan, Zhaoju Yang, and Wenbin Rui for helpful discussions and valuable comments. This work was supported by the National Key Research and Development Program of China (Grant No. 2022YFA1404201), the National Natural Science Foundation of China (NSFC) (Grant Nos. 12474361, 12034012, and 12074234), the Changjiang Scholars and Innovative Research Team in the University of Ministry of Education of China (PCSIRT)($IRT_17R70$), the Fund for Shanxi 1331 Project Key Subjects Construction, the 111 Project (D18001), and the Fundamental Research Program of Shanxi Province (Grant No. 202303021223005). Y.L. acknowledges the support from the China Association for Science and Technology (CAST), China.

# References

[1] Feng L, El-Ganainy R, and Ge L 2017 *Nat. Photon.* **11** 752
[2] El-Ganainy R, Makris K G, Khajavikhan M, Musslimani Z H, Rotter S, and Christodoulides D N 2018 *Nat. Phys.* **14** 11
[3] Yao S and Wang Z 2018 *Phys. Rev. Lett.* **121** 086803
[4] Gong Z, Ashida Y, Kawabata K, Takasan K, Higashikawa S, and Ueda M 2018 *Phys. Rev. X* **8** 031079
[5] Lee C H, Li L, and Gong J 2019 *Phys. Rev. Lett.* **123** 016805
[6] Lee C H and Thomale R 2019 *Phys. Rev. B* **99** 201103
[7] Zhang D W, Tang L Z, Lang L J, Yan H, and Zhu S L 2020 *Sci. China: Phys. Mech. Astron.* **63** 267062
[8] Bergholtz E J, Budich J C, and Kunst F K 2021 *Rev. Mod. Phys.* **93** 015005
[9] Zhang X, Zhang T, Lu M H, and Chen Y F 2022 *Adv. Phys. X* **7** 2109431
[10] Lin R, Tai T, Li L, and Lee C H 2023 *Front. Phys.* **18** 53605
[11] Wang H, Zhong J, and Fan S 2024 *Adv. Opt. Photonics* **16** 659
[12] Zhu W and Li L 2024 *J. Phys.: Condens. Matter* **36** 253003
[13] Li C A, Trauzettel B, Neupert T, and Zhang S B 2023 *Phys. Rev. Lett.* **131** 116601
[14] Manna S and Roy B 2023 *Commun. Phys.* **6** 10
[15] Weidemann S, Kremer M, Helbig T, Hofmann T, Stegmaier A, Greiter M, Thomale R, and Szameit A 2020 *Science* **368** 311
[16] Hu B, Zhang Z, Zhang H, Zheng L, Xiong W, Yue Z, Wang X, Xu J, Cheng Y, Liu X, and Christensen J 2021 *Nature* **597** 655
[17] Wang W, Wang X, and Ma G 2022 *Nature* **608** 50
[18] Zhu B, Wang Q, Leykam D, Xue H, Wang Q J, and Chong Y 2022 *Phys. Rev. Lett.* **129** 013903
[19] Yuan H, Zhang W, Zhou Z, Wang W, Pan N, Feng Y, Sun H, and Zhang X 2023 *Adv. Sci.* **10** 2301128
[20] Zhou X, Zhang W, Cao W, and Zhang X 2025 *Phys. Rev. Lett.* **135** 106601
[21] Zhou Q, Wu J, Pu Z, Lu J, Huang X, Deng W, Ke M, and Liu Z 2023 *Nat. Commun.* **14** 4569
[22] Gao Z, Qiao X, Pan M, Wu S, Yim J, Chen K, Midya B, Ge L, and Feng L 2023 *Phys. Rev. Lett.* **130** 263801
[23] Lu J, Deng W, Huang X, Ke M, and Liu Z 2025 *Adv. Mater.* **37** 2307998
[24] Sun Y, Hou X, Wan T, Wang F, Zhu S, Ruan Z, and Yang Z 2024 *Phys. Rev. Lett.* **132** 063804
[25] Lin Z, Song W, Wang L W, Xin H, Sun J, Wu S, Huang C, Zhu S, Jiang J H, and Li T 2024 *Phys. Rev. Lett.* **133** 073803
[26] Zheng X, Jalali Mehrabad M, Vannucci J, Li K, Dutt A, Hafezi M, Mittal S, and Waks E 2024 *Nat. Commun.* **15** 10881
[27] Liu G G, Mandal S, Zhou P, Xi X, Banerjee R, Hu Y H, Wei M, Wang M, Wang Q, Gao Z, Chen H, Yang Y, Chong Y, and Zhang B 2024 *Phys. Rev. Lett.* **132** 113802
[28] Guo Z, Wang Y, Ke S, Su X, Ren J, and Chen H 2024 *Adv. Phys. Res.* **3** 2470014
[29] Zhang L, Yang Y, Ge Y, Guan Y J, Chen Q, Yan Q, Chen F, Xi R, Li Y, Jia D, Yuan S Q, Sun H X, Chen H, and Zhang B 2021 *Nat. Commun.* **12** 6297
[30] Zhang X, Tian Y, Jiang J H, Lu M H, and Chen Y F 2021 *Nat. Commun.* **12** 5377
[31] Gao H, Xue H, Gu Z, Li L, Zhu W, Su Z, Zhu J, Zhang B, and Chong Y 2022 *Phys. Rev. B* **106** 134112
[32] Gu Z, Gao H, Xue H, Li J, Su Z, and Zhu J 2022 *Nat. Commun.* **13** 7668
[33] Wang W, Hu M, Wang X, Ma G, and Ding K 2023 *Phys. Rev. Lett.* **131** 207201

[34] Zhou Q, Wu J, Pu Z, Lu J, Huang X, Deng W, Ke M, and Liu Z 2023 *Nat. Commun.* **14** 4569
[35] Wan T, Zhang K, Li J, Yang Z, and Yang Z 2023 *Sci. Bull.* **68** 2330
[36] Zhang Q, Leng Y, Xiong L, Li Y, Zhang K, Qi L, and Qiu C 2024 *Adv. Mater.* **36** 2403108
[37] Li Z, Wang L W, Wang X, Lin Z K, Ma G, and Jiang J H 2024 *Nat. Commun.* **15** 6544
[38] Xiong L, Zhang Q, Feng X, Leng Y, Pi M, Tong S, and Qiu C 2024 *Phys. Rev. B* **110** L140305
[39] Wu J, Zheng R, Liang J, Ke M, Lu J, Deng W, Huang X, and Liu Z 2024 *Phys. Rev. Lett.* **133** 126601
[40] Wang Q, Fu Z, Ye L, He H, Deng W, Lu J, Ke M, and Liu Z 2025 *Phys. Rev. B* **111** L100101
[41] Wu J, Hu Y, He Z, Deng K, Huang X, Ke M, Deng W, Lu J, and Liu Z 2025 *Phys. Rev. Lett.* **134** 176601
[42] Wang S, Xiong W, Zhang Z, Cheng Y, and Liu X 2026 *Phys. Rev. Lett.* **136** 026601
[43] Helbig T, Hofmann T, Imhof S, Abdelghany M, Kiessling T, Molenkamp L, Lee C, Szameit A, Greiter M, and Thomale R 2020 *Nat. Phys.* **16** 747
[44] Hofmann T, Helbig T, Schindler F *et al.* 2020 *Phys. Rev. Res.* **2** 023265
[45] Zou D, Chen T, He W, Bao J, Lee C H, Sun H, and Zhang X 2021 *Nat. Commun.* **12** 7201
[46] Wu J, Huang X, Yang Y, Deng W, Lu J, Deng W, and Liu Z 2022 *Phys. Rev. B* **105** 195127
[47] Zhu P, Sun X Q, Hughes T L, and Bahl G 2023 *Nat. Commun.* **14** 720
[48] Zhang H, Chen T, Li L, Lee C H, and Zhang X 2023 *Phys. Rev. B* **107** 085426
[49] Xie X, Liang G, Ma F, Du Y, Peng Y, Li E, Chen H, Li L, Gao F, and Xue H 2024 *Phys. Rev. B* **109** L140102
[50] Guo C X, Su L, Wang Y, Li L, Wang J, Ruan X, Du Y, Zheng D, Chen S, and Hu H 2024 *Nat. Commun.* **15** 9120
[51] Jiang T, Zhang C, Zhang R Y, Yu Y, Guan Z, Wei Z, Wang Z, Cheng X, and Chan C 2024 *Nat. Commun.* **15** 10863
[52] Xiao L, Deng T, Wang K, Zhu G, Wang Z, Yi W, and Xue P 2020 *Nat. Phys.* **16** 761
[53] Li L, Lee C H, and Gong J 2020 *Phys. Rev. Lett.* **124** 250402
[54] Liang Q, Xie D, Dong Z, Li H, Li H, Gadway B, Yi W, and Yan B 2022 *Phys. Rev. Lett.* **129** 070401
[55] Lin Q, Yi W, and Xue P 2023 *Nat. Commun.* **14** 6283
[56] Zhao E, Wang Z, He C, Poon T F J, Pak K K, Liu Y J, Ren P, Liu X J, and Jo G B 2025 *Nature* **637** 565
[57] Shen R, Chen T, Yang B, and Lee C H 2025 *Nat. Commun.* **16** 1340
[58] Li Y, Liang C, Wang C, Lu C, and Liu Y C 2022 *Phys. Rev. Lett.* **128** 223903
[59] Huang X, Li Y, Zhang G F, and Liu Y C 2024 *Phys. Rev. A* **109** L021503
[60] Tang Y, Wu J, Lai P, Hu Y, Liu H, Deng W, Cheng H, Liu Z, and Chen S 2025 *Nat. Commun.* **16** 10420
[61] Aidelsburger M, Nascimbene S, and Goldman N 2018 *C. R. Phys.* **19** 394
[62] Zhang D W, Zhu Y Q, Zhao Y, Yan H, and Zhu S L 2018 *Adv. Phys.* **67** 253
[63] Shao L, Zhu S L, Sheng L, Xing D, and Wang Z 2008 *Phys. Rev. Lett.* **101** 246810
[64] Yuan L, Shi Y, and Fan S 2016 *Opt. Lett.* **41** 741
[65] Yuan L, Lin Q, Xiao M, and Fan S 2018 *Optica* **5** 1396
[66] Song W, Yang Y, Lin Z *et al.* 2025 *Nat. Rev. Phys.* **7** 606
[67] Zhang D W, Wang Z D, and Zhu S L 2012 *Front. Phys.* **7** 31
[68] Liang Q, Dong Z, Pan J S, Wang H, Li H, Yang Z, Yi W, and Yan B 2024 *Nat. Phys.* **20** 1738
[69] Cheng D, Wang K, Roques-Carmes C, Lustig E, Long O Y, Wang H, and Fan S 2025 *Nature* **637** 52
[70] Zhu S L, Fu H, Wu C J, Zhang S C, and Duan L M 2006 *Phys. Rev. Lett.* **97** 240401
[71] Chen Z, Yang S A, and Zhao Y 2022 *Nat. Commun.* **13** 2215
[72] Ma S, Jia H, Bi Y, Ning S, Guan F, Liu H, Wang C, and Zhang S 2023 *Phys. Rev. Lett.* **130** 243801
[73] Zhang J H, Mei F, Xiao L, and Jia S 2024 *Phys. Rev. Lett.* **132** 036603
[74] Zhang J H, Mei F, Li Y, Lee C H, Ma J, Xiao L, and Jia S 2025 *Nat. Commun.* **16** 2050
[75] Qian H, Gong M, Zhang J *et al.* 2025 *Science* **390** 930
[76] Xue H, Chen Z, Cheng Z, Dai J, Long Y, Zhao Y, and Zhang B 2023 *Nat. Commun.* **14** 4563
[77] Zhao W, Zheng Y, Lu C, Wang Z, Liu Y C, and Zhang S 2024 *Phys. Rev. Lett.* **133** 233801
[78] Li H, Dong Z, Longhi S, Liang Q, Xie D, and Yan B 2022 *Phys. Rev. Lett.* **129** 220403
[79] Zhang W, Wang H, Sun H, and Zhang X 2023 *Phy. Rev. Lett.* **130** 206401
[80] Wang H, Zhang W, Sun H, and Zhang X 2023 *Phys. Rev. B* **108** 144203
[81] Fang K and Fan S 2013 *Phys. Rev. Lett.* **111** 203901
[82] Yang Y, Ge Y, Li R, Lin X, Jia D, Guan Y j, Yuan S q, Sun H x, Chong Y, and Zhang B 2021 *Sci. Adv.* **7** eabj2062
[83] Song W, Li T, Wu S, Wang Z, Chen C, Chen Y, Huang C, Qiu K, Zhu S, Zou Y, and Tao L 2022 *Phys. Rev. Lett.* **129** 053901
[84] Lin Q and Fan S 2014 *Phys. Rev. X* **4** 031031
[85] Mittal S, Fan J, Faez S, Migdall A, Taylor J, and Hafezi M 2014 *Phys. Rev. Lett.* **113** 087403
[86] Yuan L and Fan S 2015 *Phys. Rev. Lett.* **114** 243901
[87] Rui W, Zhao Y, and Wang Z 2023 *Phys. Rev. Lett.* **131** 176402
[88] Zhang K, Yang Z, and Fang C 2022 *Nat. Commun.* **13** 2496
[89] Qin Y, Zhang K, and Li L 2024 *Phys. Rev. A* **109** 023317
[90] Kawabata K, Sato M, and Shiozaki K 2020 *Phys. Rev. B* **102** 205118
[91] Lee C H, Imhof S, Berger C, Bayer F, Brehm J, Molenkamp L W, Kiessling T, and Thomale R 2018 *Commun. Phys.* **1** 39
[92] Imhof S, Berger C, Bayer F, Brehm J, Molenkamp L W, Kiessling T, Schindler F, Lee C H, Greiter M, Neupert T, and Thomale R 2018 *Nat. Phys.* **14** 925
[93] Yang H, Song L, Cao Y, and Yan P 2024 *Phys. Rep.* **093** 1
[94] Chen T, Zhang W, Zou D, Sun Y, and Zhang X 2025 *Adv. Quantum Technol.* **8** 2400448
[95] Sahin H, Jalil M B A, and Lee C H 2025 *APL Electron. Devices* **1** 021503